CrossMark

Parylene MEMS patency sensor for assessment of hydrocephalus shunt obstruction

Brian J. Kim[1] · Willa Jin[1] · Alexander Baldwin[1] · Lawrence Yu[1] · Eisha Christian[2] ·
Mark D. Krieger[2,3] · J. Gordon McComb[2,3] · Ellis Meng[1,4]

Abstract Neurosurgical ventricular shunts inserted to treat hydrocephalus experience a cumulative failure rate of 80 % over 12 years; obstruction is responsible for most failures with a majority occurring at the proximal catheter. Current diagnosis of shunt malfunction is imprecise and involves neuroimaging studies and shunt tapping, an invasive measurement of intracranial pressure and shunt patency. These patients often present emergently and a delay in care has dire consequences. A microelectromechanical systems (MEMS) patency sensor was developed to enable direct and quantitative tracking of shunt patency in order to detect proximal shunt occlusion prior to the development of clinical symptoms thereby avoiding delays in treatment. The sensor was fabricated on a flexible polymer substrate to eventually allow integration into a shunt. In this study, the sensor was packaged for use with external ventricular drainage systems for clinical validation. Insights into the transduction mechanism of the sensor were obtained. The impact of electrode size, clinically relevant temperatures and flows, and hydrogen peroxide (H_2O_2) plasma sterilization on sensor function were evaluated. Sensor performance in the presence of static and dynamic obstruction was demonstrated using 3 different models of obstruction. Electrode size was found to have a minimal effect on sensor performance and increased temperature and flow resulted in a slight decrease in the baseline impedance due to an increase in ionic mobility. However, sensor response did not vary within clinically relevant temperature and flow ranges. H_2O_2 plasma sterilization also had no effect on sensor performance. This low power and simple format sensor was developed with the intention of future integration into shunts for wireless monitoring of shunt state and more importantly, a more accurate and timely diagnosis of shunt failure.

Keywords Patency · Sensor · Parylene C · Hydrocephalus · Obstruction

1 Introduction

Hydrocephalus is a condition characterized by accumulation of excess cerebrospinal fluid (CSF) within the ventricles of the brain, due to an imbalance in the production and drainage of CSF. If left untreated, it can lead to neurological defects, severe brain damage, and death. The etiology of hydrocephalus can be either congenital or acquired; there are multiple causes such as congenital malformations, tumor, trauma, meningitis, and hemorrhage (Pople 2002). Since the 1950s, hydrocephalus has been largely treated by the insertion of a shunt system consisting of a multi-pore silicone proximal catheter, mechanical valve, and a silicone distal catheter designed to drain excess CSF out of the ventricles (Baru et al. 2001). More specifically, the proximal catheter, placed within the ventricle, is connected to a pressure- or flow-controlled one-way valve (either a set pressure or programmable valve) that directs the fluid out of the ventricle and through the distal catheter and

✉ Ellis Meng
ellis.meng@usc.edu

[1] Department of Biomedical Engineering, Viterbi School of Engineering, University of Southern California, 1042 Downey Way, DRB-140, Los Angeles, CA 90089-1111, USA

[2] Department of Neurological Surgery, Keck School of Medicine, University of Southern California, 1200 North State St., Suite 3300, Los Angeles, CA 90033, USA

[3] Division of Neurosurgery, Children's Hospital Los Angeles, 4650 Sunset Blvd., MS #102, Los Angeles, CA 90027, USA

[4] Ming Hsieh Department of Electrical Engineering, Viterbi School of Engineering, University of Southern California, 3651 Watt Way, VHE-602, Los Angeles, CA 90089-0241, USA

drains CSF either into the peritoneal cavity (ventriculoperitoneal shunt), pleural cavity (ventriculopleural shunt), or the atrium of the heart (ventriculoatrial shunt) where CSF is reabsorbed.

Though effective, shunts fail at an alarming rate of 40 % within the first year and up to 80 % within ten years (Drake et al. 2000). There are many causes of shunt failure, including mechanical (i.e. hardware-related) issues (Browd et al. 2006) and infection (Kulkarni et al. 2001), but the most common is obstruction of the drainage ports (70 % of cases) (Drake et al. 1998; Kestle et al. 2000; Browd et al. 2006; Haberl et al. 2009). Although obstruction of the shunt cannot be attributed to a single cause, ingrowth or attachment of choroid plexus tissue, inflammatory cells, blood components, and other cellular debris all contribute to obstructive shunt failure (Brydon et al. 1998; Dickerman et al. 2005; Browd et al. 2006; Thomale et al. 2010; Harris and McAllister 2012; Blegvad et al. 2013). This cellular and tissue attachment has been attributed to the typical foreign body response for implants exacerbated by the disruption of the blood-brain barrier upon implantation (Lundberg et al. 1999; Harris and McAllister 2012; Blegvad et al. 2013), an increase in shear stress around high flow regions (i.e. at the holes) (Harris et al. 2010; Harris and McAllister 2011), and proximity to tissue structures (i.e. improper placement of the shunt) (Kaufman and Park 1999; Tuli et al. 1999; Lin et al. 2003; Thomale et al. 2010; Blegvad et al. 2013). Shunt failures may cause severe symptoms and may require emergent shunt revision surgery (Wong et al. 2012).

There are currently no reliable and convenient methods to predict shunt obstruction. Obstruction may result in vague, nonspecific symptoms, such as headaches and nausea, which can be easily misdiagnosed or may present acutely with the need for emergent intervention. The current clinical standard to assess shunt state is the use of static imaging of the brain (i.e., magnetic resonance imaging (MRI), computed tomography (CT) scans) for initial analysis and may be followed by an invasive shunt tap procedure, in which a needle is punctured through the skin into a reservoir within the implanted reservoir to assess CSF flow. These methods are imprecise, largely based on the clinician's expertise. Given the high incidence of shunt failure and associated risks to the patient, hydrocephalus treatment could be improved through the development of a "smart shunt" that can periodically assess shunt operation and accurately identify the warning signs of impending shunt failure with the use of integrated sensors (Lutz et al. 2013).

Towards this aim, we introduce a Parylene-based electrochemical (EC) sensing approach that directly interfaces with the wet *in vivo* environment and integrates with existing shunt systems. The use of a Parylene C substrate allows for batch fabrication of sensors with great reproducibility and dimensional accuracy due to Parylene C's compatibility with micromachining processes, as well as substrate flexibility to facilitate packaging of identical sensor systems into many different connection schemes (e.g. an implantable module for use in implanted shunt systems, or a larger module for use in external ventricular drains (EVD)). Parylene C's proven track record in biomedical applications as a United States Pharmacopeia (USP) class VI material also makes it an ideal candidate for construction of a medical implant. This sensor utilizes a very simple transduction scheme to assess the degree of shunt patency by measuring changes in electrochemical impedance in the conductive path through the drainage ports in the shunt catheter. This sensor will enable quantitative monitoring of shunt performance and more importantly, provide accurate and timely diagnosis of failure to improve treatment for hydrocephalus patients. In this paper, we present the development and characterization of the MEMS patency sensor.

2 Design and operation

The sensing mechanism selected is straightforward and inspired by previous EC-MEMS sensors (Gutierrez and Meng 2011; Kim et al. 2012; Sheybani et al. 2012) as well as the Coulter counter principle (Coulter 1956). Patency of a drainage port is monitored by measuring the impedance between a pair of electrodes immersed in an electrolyte solution (Fig. 1a). Two electrodes are positioned on each internal and external surfaces of the catheter, such that the catheter ports establish an ionic conductive path between them (Fig. 1b).
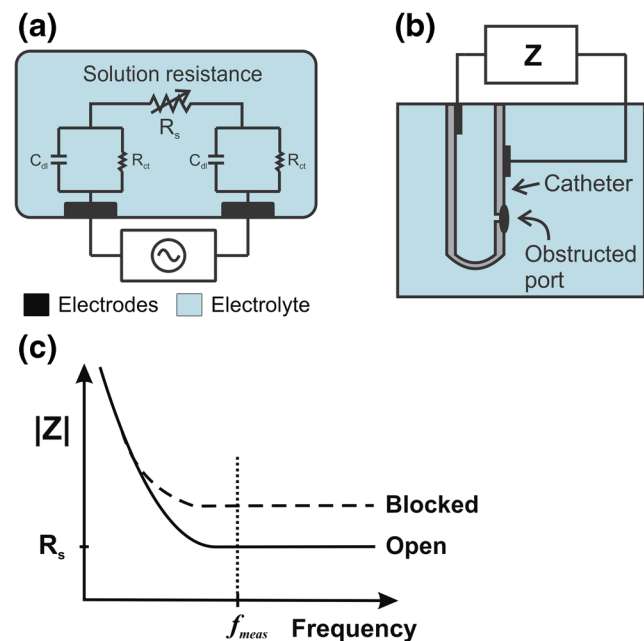

Fig. 1 **a** Equivalent circuit model of two electrodes in an electrolyte, highlighting the solution resistance. **b** Conceptual cartoon of impedance sensing mechanism of patency sensor. Two electrodes on the internal and external surfaces of the catheter are fluidically connected via the drainage ports. Obstruction of these ports impedes the ionic conduction path between the electrodes, and **c** the electrochemical impedance between the electrodes increases for measurements above a certain frequency (f_{meas})

When measuring the electrochemical impedance at a sufficiently high frequency (f_{meas}) to isolate the solution resistance (R_s), any disturbances in the volumetric conduction path between the two electrodes (i.e. port blockage) will register as changes in the measured impedance (Fig. 1c).

In this configuration, the sensor effectively acts as a variable resistor and changes in the measured resistance following Eq. 1 can be attributed to either (1) the resistivity of the solution (i.e. the ionic concentration of the solution) (ρ), (2) the cross sectional area between the electrodes (A), or (3) the distance between the electrodes (l).

$$Z \approx R_s = \frac{\rho l}{A}; \quad \text{for sufficiently high } f_{meas} \tag{1}$$

A decrease in the number of open drainage ports in the catheter, a consequence of shunt obstruction, will decrease the available cross sectional area between the pair of electrodes, closing off available conductive paths. Thus, we expect that the relationship between measured impedance and obstruction should follow an inverse relationship (i.e. 1/A) per Eq. 1.

A similar approach was also developed within literature in the use of integrated ring electrodes on the internal surface of ventricular catheters that found success in preliminary studies correlating impedance changes with cellular ingrowth into the catheter (Basati et al. 2014). This electrode orientation however was shown to only be sensitive to the presence of cellular growth within the catheter and can be greatly be improved by moving one of the electrodes to the outer surface of the catheter (as presented here), which can improve its sensitivity to a larger variety of shunt obstructive phenomena, such as sheathing-type blockages of the catheter that are contained to the outside surface of the catheter. Also, the device design does not allow it to integrate with current shunt systems, but rather replace them, which can cause delays in adoption and use within hospitals. Despite this, the developed approach shows the promise of utilizing impedance as a sensing mechanism for applications within improving hydrocephalus treatment.

3 Fabrication and packaging

The patency sensor was constructed using standard surface micromachining processes for Parylene MEMS devices (Meng et al. 2008; Meng et al. 2011). Platinum (Pt) electrodes (2000 Å) were e-beam evaporated and patterned using the liftoff method on a Parylene C substrate (12 μm) deposited on a silicon carrier wafer. Pt was chosen as it has shown outstanding inertness for *in vivo* and electrochemical sensing applications (Nam 2012). The electrodes were insulated by depositing another layer of Parylene C (12 μm) and electrode sites were exposed via oxygen plasma etching. The final device was released by a complete cut out etch in oxygen plasma (Fig. 2).

Free film sensor dies were released from the carrier wafer by first stripping the protective photoresist mask used during the final release etch, and then gentle peeling using tweezers; immersing the wafer in deionized (DI) water facilitated the process. Released devices were electrically packaged by fitting the contact pad end of the sensor dies into a zero-insertion-force (ZIF) connector (12 channel, 0.5 mm pitch; Hirose Electric Co., Simi valley, CA) soldered onto a flat flexible cable (FFC; Molex Inc., Lisle, IL), a commonly used technique for Parylene devices (Gutierrez et al. 2011) (Fig. 3). As the ZIF connector requires an inserted cable of a certain thickness and stiffness, the contact pad regions of the Parylene device were affixed to a poly(etheretherketone) (PEEK) stiffener backing (300 μm) prior to insertion into the connector. The ZIF connector region was encapsulated in EpoTek 353-NDT biocompatible epoxy (Epoxy Technology, Inc., Billerica, MA), before further assembly into the module (Fig. 3b).

The electrically packaged sensor was then inserted into one of two different luer-lock compatible fittings (cap and inline configurations) intended for integration into an EVD system (Fig. 4) for acute validation studies in humans, a critical step towards the development of an implantable sensor module. For the cap module, the Parylene device was first affixed within a slit of a rubber stopper on top of a cap housing using EpoTek 353-NDT biocompatible epoxy (Epoxy Technology, Inc., Billerica, MA), which was then filled with artificial CSF (aCSF). A 3-way valve system allowed for attachment of the cap module to the rest of the testing system. In a second
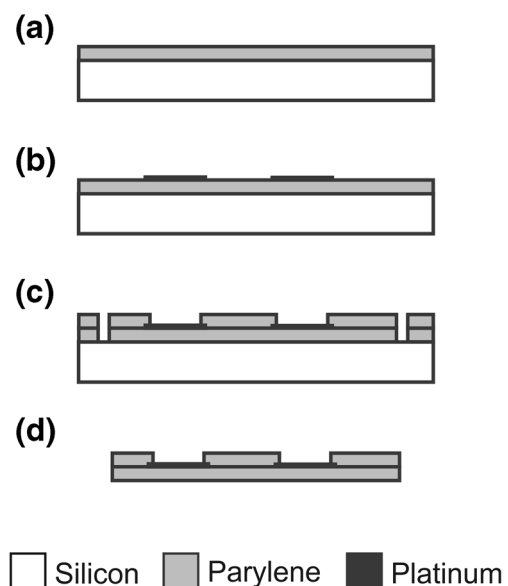

Fig. 2 Process flow for fabrication of Parylene patency sensor. **a** Parylene C (12 μm) is deposited on a silicon carrier wafer. **b** Pt electrodes (2000 Å) are deposited via e-beam evaporation and patterned using liftoff. **c** An insulation layer of Parylene C (12 μm) is deposited and electrode sites and final device shape are realized using oxygen plasma etching. **d** Devices are released from wafer by gentle peeling while immersed within DI water
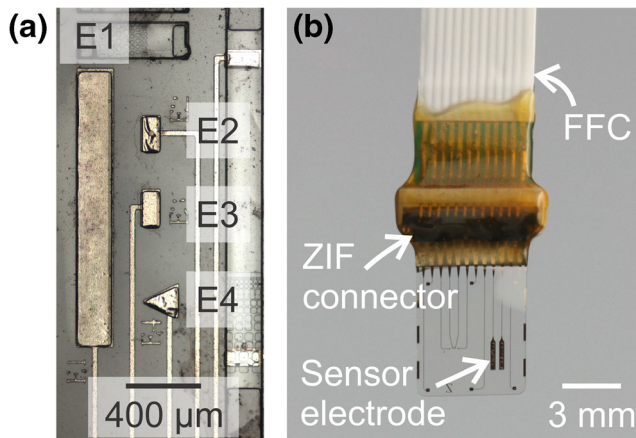
Fig. 3 **a** Optical micrograph of Parylene device with 4 electrode designs to determine the electrode size effect on performance. **b** Electrically packaged Parylene device with final electrode design using a ZIF connector and integrated flat flexible cable (FFC). Biocompatible epoxy (yellow) was added for encapsulation

arrangement, the inline module was formed by affixing the sensor platform within a milled slit in a luer-lock connector (80,379, QOSINA, Edgewood, NY) using EpoTek 353-NDT biocompatible epoxy (Epoxy Technology, Inc., Billerica, MA). The inline design removed the need to prefill the module with aCSF and simplified integration with the drainage system by eliminating the extra 3-way valve component, which had issues with bubbles at attachment ports. In both modules, the integrated FFC was used as the connection scheme to the impedance measurement system.

Initially, four electrodes having different surface areas were fabricated on a single device packaged within the cap module to evaluate effects of electrode size on sensor performance. The final device with a single electrode size device and packaged in a luer lock module was used for all subsequent testing and characterization.

4 Methods

For benchtop testing, blockage of the catheters was simulated by mock silicone catheters with varying numbers of open
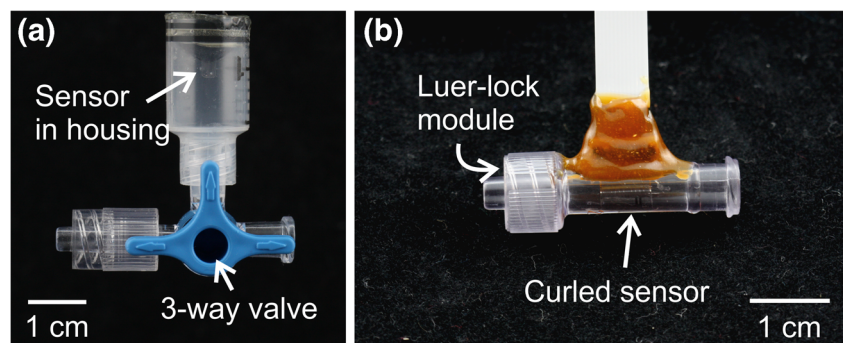
holes; 16 holes simulated the 100 % open condition (a 4-holed catheter would be classified as 75 % blockage, 8 holes as 50 %, etc.) (Fig. 5a) (Harris and McAllister 2011). Mock catheters were constructed by sealing one end of a silicone tube (1.5 mm ID) with cured silicone and manually punching holes with a 15 gauge coring needle to create 1 mm diameter holes, similar to those of a Medtronic proximal catheter (Becker® EDMS Ventricular Catheter, Medtronic, Minneapolis, MN) for use in hydrocephalus shunt systems.

The catheter was then placed within a beaker of aCSF [ionic formulation for 1 L of DI water: 8.66 g NaCl, 0.224 g KCl, 0.206 g $CaCl_2 \cdot 2H_2O$, 0.163 g $MgCl_2 \cdot 6H_2O$, 0.214 g $Na_2HPO_4 \cdot 7H_2O$, 0.027 g $NaH_2PO_4 \cdot H_2O$] and connected to the sensor module using a 1/16″ barb-to-luer connector. The assembly was filled via a syringe or peristaltic pump (for static and flow conditions, respectively) prior to testing (Fig. 5b). A platinum wire electrode was placed within the beaker to close the circuit and complete the sensing setup. Impedance measurements were acquired using a Gamry R600 potentiostat for experiments requiring measurement over a frequency range for initial characterization, or an Agilent e4980a (1 Vp-p., 10 kHz; Agilent Technologies, Santa Clara, CA) or HP/ Agilent 4285a (1 Vp-p., 75 kHz; Agilent Technologies, Santa Clara, CA) for measurements at a single frequency.

A series of benchtop characterization experiments of the Parylene patency sensor were conducted. First, the f_{meas} that isolates the solution resistance within the sensor's impedance response was determined in order to obtain the optimal sensing performance for patency. Then sensor sensitivity measurements were performed to assess the relationship between measured electrochemical impedance and number of open holes (i.e. percent shunt blockage). These experiments were conducted using four electrode sizes all fabricated on a single device to evaluate electrode size effects on sensor performance.

In the final device, a single electrode size was selected based on the experimental data and a new set of sensors were fabricated to allow characterization in simulated *in vivo* conditions. The effects of clinically relevant patient temperatures as well as possible flow rates within the shunt systems were evaluated. The effect of temperature on sensor performance was evaluated by using a hot plate to maintain the beaker of

Fig. 4 Fluidically packaged sensors in **a** cap and **b** inline modules used for benchtop testing. The inline module was designed for sensor integration with external ventricular drainage systems for clinical validation studies. In this form factor, sensors are curled within the lumen, lying snug against to the interior lumen wall to permit uninterrupted flow
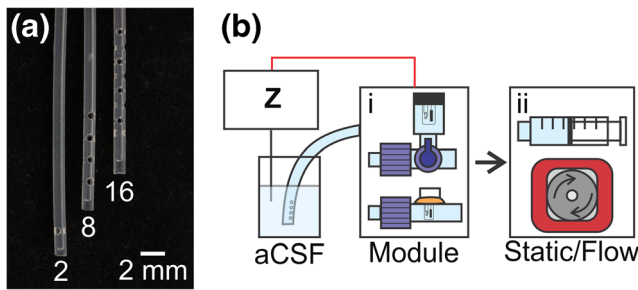
Fig. 5 **a** Mock silicone catheters (ID =1 mm) with varying number of holes (Ø = 1 mm) used for benchtop testing. **b** Experiments were conducted using either the (i) cap or inline module with a (ii) syringe or peristaltic pump for static and flow conditions, respectively. Impedance was measured between the sensor electrode and platinum ground electrode in the beaker

aCSF at a constant temperature between 32 and 44 °C. A temperature probe was placed within the aCSF solution to record the temperature. Flow was generated in the system by connecting the inline module to a peristaltic pump (WM 120 U DM3, Watson Marlow, Wilmington, MA). A 0.38 mm bore tubing was chosen for use with the peristaltic pump to provide physiologically relevant flow conditions: 0.03–0.6 mL/min at 120 pulses/min (Harris et al. 2010). Functionality of the devices following hydrogen plasma (H$_2$O$_2$) sterilization, a commonly used sterilization technique for heat-sensitive equipment in hospitals, performed with a Sterrad 100 NX system (Advanced Sterilization Products, Irvine, CA) was also assessed to examine performance post-sterilization. Additional benchtop studies of sensor drift were also conducted using a "bottle brain" benchtop model

consisting of a closed bottle system with external pressure control, and ports for catheter input and a Pt ground wire.

The dynamic blockage performance of the integrated patency sensors was also assessed by continuously measuring shunt patency via the integrated sensor during various models of progressive blockage: (1) catheter indentation experiments to pinch off the fluidic pathway to mimic a blockage of the lumen of the catheter, (2) sheathing-unsheathing experiments of a catheter using larger diameter tubing to model drainage port blockage, and (3) polyethylene glycol (PEG) dissolution of catheter holes in a "reverse" obstruction experiment to model expected *in vivo* obstructive phenomena (both lumen and sheathing blockage).

5 Results and discussion

5.1 Electrode size characterization

Impedance measurements were conducted at frequencies between 0.1 Hz – 1 MHz and the magnitude and phase as a function of frequency are presented in Fig. 6a and b, respectively. An optimal f_{meas} was determined for each sensor size (Table 1). Impedances at frequency ranges greater than f_{meas}, corresponding to where the solution resistance dominates the impedance response, correlated well with simulated catheter blockage.

By analyzing the data for each electrode at its corresponding optimal measurement frequency, calibration curves ("patency curves") were generated and results indicated that the impedance varied inversely with the number of open holes

Fig. 6 **a** Electrochemical impedance spectroscopy results of the impedance magnitude of the E1 electrode indicating variations for measurements frequencies >10 kHz between different catheter blockages. **b** Electrochemical impedance spectroscopy results of the impedance phase of the four electrode sizes demonstrating varying optimal measurement frequencies (where phase = 0°). **c** Patency curve obtained for the E1 electrode within the cap module indicating an inverse relationship between measure impedance magnitude and the number of open holes (percent blockage)
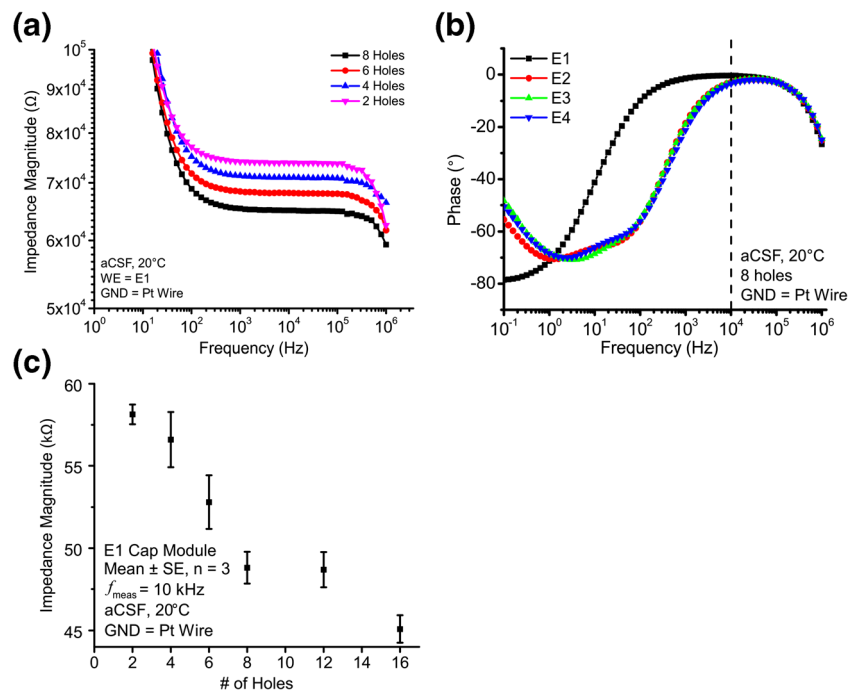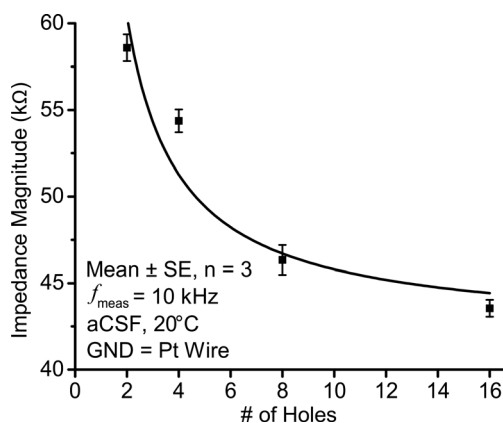
Table 1 Obtained optimal impedance measurement frequencies and sensitivities for electrodes of the Parylene-based EC-MEMS patency sensor

Electrode design	Surface area (μm^2)	Optimal measurement frequency (kHz)	Sensitivity ($\%\Delta Z$ / %Blockage)
E1	300,000	10	0.183
E2	20,000	30	0.157
E3	20,000	30	0.168
E4	17,320	30	0.161

(percent blockage) of the catheter (Fig. 6c). These results suggest that increasing catheter hole obstructions alter the cross sectional area term of Eq. 1 as hypothesized; reducing the number of open holes reduces the available conduction paths between the pair of electrodes and thus increases the impedance. In analyzing the results, though all electrode sizes were similar in performance, the largest electrode (E1) was chosen as the final design moving forward as: (1) the sensitivity was slightly higher than the others (0.183 %Δimpedance/% blockage) and (2) a larger electrode surface area has been shown to reduce noise and drift for electrochemical impedance measurements (Sheybani et al. 2012). In all subsequent experiments, f_{meas} was set as 10 kHz for the E1 electrode.

5.2 Sensor characterization

Characterization experiments with the inline module packaged device determined that the newly designed and packaged patency sensor performed identically to the E1 electrodes in the electrode size calibration devices. The cured biocompatible epoxy to seal the device within the module was qualitatively tested under pressure for air or liquid leaks by subjecting the inline module to nitrogen pressure in empty and liquid filled cases. No air leaks were observed up to 1500 mmHg (limit of the experimental setup) and no liquid leaks were

Fig. 7 Patency curve obtained for a sensor within inline module confirming a similar trend to results obtained with the E1 electrode within the cap module

observed up to 100 mmHg, both considerably higher than the expected pressure ranges within the brain (0–25 mmHg).

Patency curves for these devices retained an inverse relationship and a similar sensitivity observed in previous experiments, demonstrating an increase of ~27 % impedance magnitude increase for a 87.5 % (2 holes open) blockage (Fig. 7). In an analysis of the sensor response, the variation in measurement was determined to be 100–200 Ω, which is within the resolution of the measurement system. Using the high precision LCR meters (e4980a and 4285a) for benchtop testing, the devices can resolve 0.2 % of the baseline impedance (100–200 Ω), which correlates to 2–3 % obstruction. Further *in vivo* testing is necessary to correlate a patency sensor measurement with what would qualify as a clinical shunt obstruction failure. But currently, complete obstruction of the catheter results in a sensor reading of 3.58 MΩ, which is >8000 % increase in measured impedance.

5.3 Hole position dependency

When simulating catheter obstruction in benchtop experiments, mock catheters were fabricated to model hole obstruction in a specific direction, with simulated blockages occurring from the top (i.e. "proximal" to the sensor) downwards (i.e. "distal" to the sensor) (Fig. 8a). In an experiment where the order of obstruction was reversed, such that the blockage occurred from the distal-end proximally (i.e. bottom-up) (Fig. 8a), decreased sensitivity was observed even though the total number of open holes remained the same (Fig. 8b). Closer analysis of the results indicated that for the 2, 4, 6, and 8-holed catheters within the "Reversed" catheter set, measured impedances demonstrated similar values as long as the most proximal hole was in the same position and was patent. This follows from a "path of least resistance" effect, where a majority of the ionic conduction path between the two electrodes is contributed across the nearest opening (i.e. the most proximal hole). This result revealed that the sensor predominantly monitors the patency (or position) of the hole closest to it.

This result was confirmed in another experiment exploring two different catheter sets with varying hole orientations. In the first set ("Normal"), mock catheters were constructed such that the total number of open holes were 2, 4, 8, and 16 (Fig. 9a). In the second set ("Alternate"), mock catheters were constructed with a total number of open holes of 2, 6, 14, and 16, as shown in Fig. 9b. It is important to note that when comparing the 4-holed catheter from the Normal set and the 6-holed catheter from the Alternate set, while the total number of open holes is different, the most proximal hole in each catheter is in the same position. An analogous comparison can be made for the 8 and 14-holed catheters from the Normal set and Alternate set, respectively. When looking at the patency curves for these two sets of catheters, a similar impedance value is recorded between the catheters with
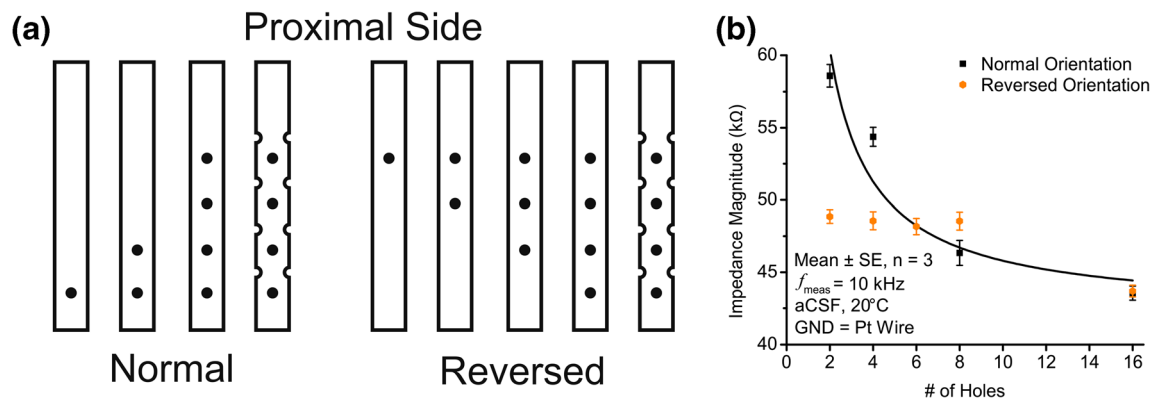
Fig. 8 **a** Two different catheter hole orientations (Normal and Reversed) used to assess the transduction mechanism of the sensor. Each solid hole indicates two open holes in the mock catheter. **b** Resultant patency curves of the two catheter orientations indicate that the sensor was not measuring the total number of open holes, but rather only the position of the most proximal open hole, following a "path of least electrochemical resistance" effect

identical proximal hole positions due to the "path of least resistance" effect as described previously (Fig. 9b).

It follows that the patency curves for the sensor depend largely on the obstruction model for the mock catheters; if the obstruction occurs in a linear manner, e.g. from the most proximal hole towards the distal end of the catheter, then the patency curve is linear. This conclusion adjusts the sensing mechanism, such that the variable parameter in Eq, 1 for this sensing mechanism is the l, or the distance between the electrodes, and not the A term. Therefore, in evaluating the sensing mechanism of the patency sensor for these catheters, the only hole of importance is the most proximal (i.e, closest to the sensor) hole, the remaining holes have marginal impact on electrochemical impedance. Thus obstruction events from the most proximal hole to the distal end of the catheter merely extend the ionic conduction path (and thus distance) between the two electrodes.

Fortunately, benchtop studies in literature have found that 80 % of the flow through the catheters occurs at these proximal holes (Lin et al. 2003; Thomale et al. 2010). The high flow (Lin et al. 2003) and greater shear stresses (Harris et al. 2010; Harris and McAllister 2011; Harris et al. 2011) that occur across these holes also greatly increases the likelihood of obstruction at this site. These results were confirmed in benchtop flow studies with colored dye using the mock catheter system; bulk flow only through the most proximal hole was qualitatively confirmed (Fig. 10). Though these results may vary for chronically implanted catheters, these results are promising. Monitoring the top hole may be critical if not sufficient for assessing shunt patency. In addition, this sensor orientation is optimal for tracking other clinical phenomena that may occur during the implantation or lifetime of the shunt catheter, namely assessing improper placement of the shunt where the top-most hole is placed right next to the ventricular
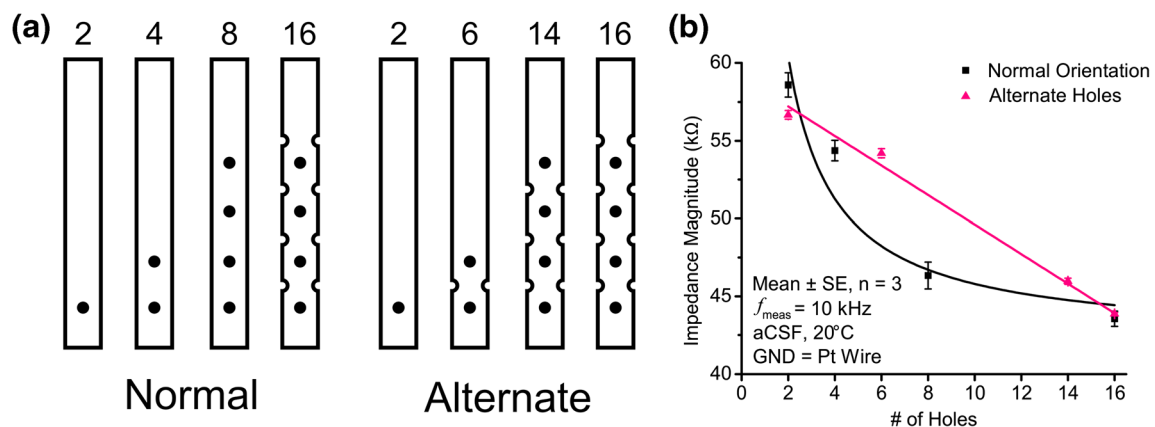

Fig. 9 **a** Two different catheter sets (Normal and Alternate) used to assess the dependency of the sensor response on the most proximal open hole. Total open holes are given above each catheter drawing. Note that each catheter between the sets has the same proximal open hole position but a different number of total open holes (e.g. 4 holed-catheter of the Normal set has the same top-most hole position of the 6-holed catheter in the Alternate set). **b** Resultant patency curves of the two catheter sets indicate that even with varying number of total open holes, the measured impedance is dependent only on the most proximal hole, following a "path of least resistance" effect, and thus a more linear response in the case for blockages from the top of the catheter downwards
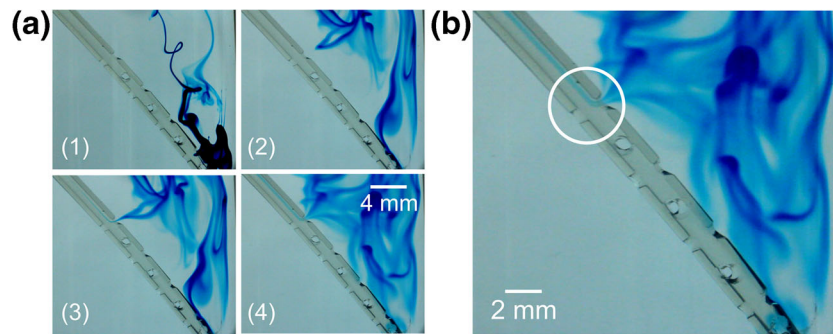
Fig. 10 a Time-lapse images (1 → 4) of a dye drop experiment into a 16-holed catheter within aCSF under flow (0.3 mL/min). Note that though the dye was placed at the bottom holes, a blue dye stream is not observed until the diffused dye reaches the top hole (image 3). Even in image 4,

though the dye is within the proximity of the other holes, dye flow is still only observed through the most proximal hole. **b** Magnified image of catheter illustrating the blue flow stream into the catheter only at the most proximal hole (white circle)

wall (Kaufman and Park 1999; Lin et al. 2003; Thomale et al. 2010), or ventricular size changes during treatment and subsequent catheter movement (e.g. slit or borderline slit ventricles) (Harris and McAllister 2012; Blegvad et al. 2013). Both phenomena have been shown to correlate with the most proximal hole obstructed in explanted catheters.

5.4 Thermal effects

Patency curves for the inline module for aCSF solution temperatures between 32 and 44 °C indicated a reduction in baseline impedances largely due to increased ionic mobility and decreased solution viscosity (i.e. increased conductivity of the solution) at elevated temperatures (Fig. 11a), similar to the temperature effect observed in the measurement of resistance. The temperature coefficient of resistance (TCR) calculated for the Parylene patency sensor was −287.7 Ω/°C within this benchtop system. Experiments that explored more clinically relevant hydrocephalic patient temperatures (34–38 °C) indicated no large variations for baselines for the patency curves for the inline module (Fig. 11b). These devices are largely insensitive to patient temperature swings, as expected impedance increases due to shunt obstructive failure are much higher than a slight decrease in baseline.
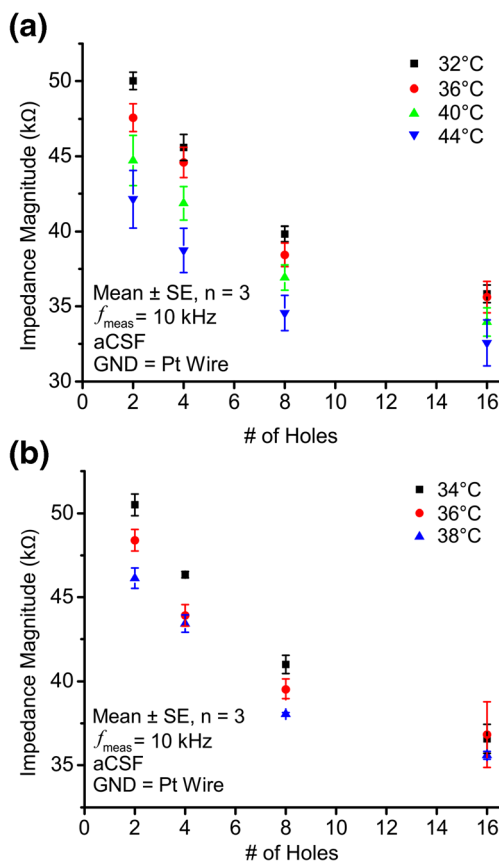
5.5 Flow effects

Similar to observed effects for increased temperatures, the presence of flow within the system (and thus across the sensor

Fig. 11 a Patency curves obtained for the inline modules for varying temperatures 32–44 °C, indicating a decrease in baseline, but retaining a similar sensitivity. **b** Within clinically relevant temperatures between 34 and 38 °C, no large variations were recorded
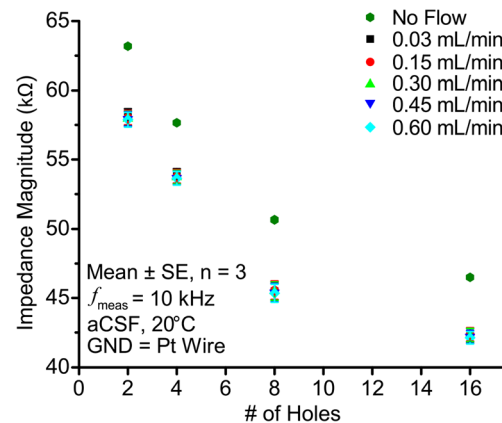

Fig. 12 Patency curves measured for inline modules indicate that there is a decrease in impedance of ~8 % with the addition of flow, but no variation among flow rates within the range of 0.03–0.6 mL/min
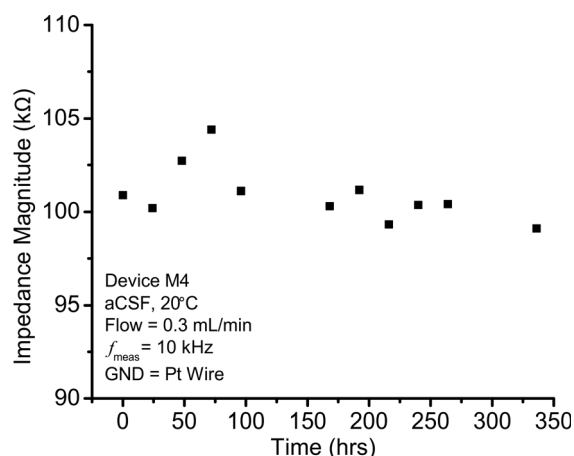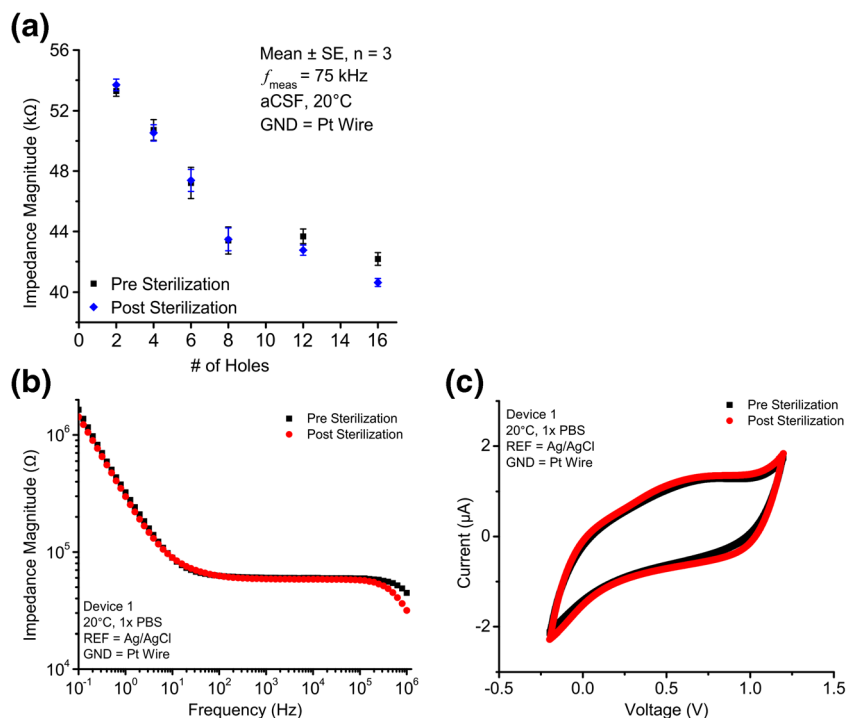
Fig. 13 Measured impedance of patency sensor for a 16-holed catheter in a bottle brain within flow for 14 days demonstrating low drift of the sensor response

electrodes) reduced the baseline impedance (~8 %) largely due to an increase in ionic mobility (Fig. 12). The use of electrochemical impedance to measure fluid flows has been demonstrated within literature and the sensitivies of impedance to flow largely depend on the electrode orientations (Ayliffe and Rabbitt 2003). For the inline module, the specific electrode orientation as parallel to the fluid flow as well as the relatively long distance (>7 cm apart) resulted in similar sensor responses at clinically relevant flow ranges 0.03–0.60 mL/min (Bork et al. 2010) (Fig. 12). Thus the sensor is also largely insensitive to various flow speeds, but is sensitive to the presence of flow or the absence of flow.

5.6 Drift experiments

Long term drift experiments were carried out using the bottle brain system for two weeks at room temperature to look for any prevailing trends in the baseline signal of the devices. A 16-holed mock silicone catheter, placed inline with the sensor module using a 1/16″ barb connector, was placed within the aCSF-filled bottle brain (20 °C) along with a ground Pt wire electrode. Flow out of the catheter was established using a peristaltic pump set at 0.3 mL/min. Impedances were measured in 24 h increments for 14 days. An experiment end time of 14 days was chosen to validate the sensor response over the planned time for future clinical validation studies with the EVD system. Impedance varied ±3.5 % during the 14 days, largely due to the presence of bubbles within the system on the third and fourth days (Fig. 13). These results are promising, and this minor variation compares favorably to the expected sensor response due to obstruction, an impedance increase of ~30 %. Future *in vivo* studies for longer time periods will confirm the stability of the sensor reading for chronic applications.

5.7 Sterilization effects

H_2O_2 plasma sterilization of inline module packaged device was conducted at Children's Hospital Los Angeles per institutional protocols for sterilization of their medical hardware using a Sterrad 100 NX system. Patency curves following sterilization indicated that sensor performance remained unaltered (Fig. 14a). Electrode characterization using
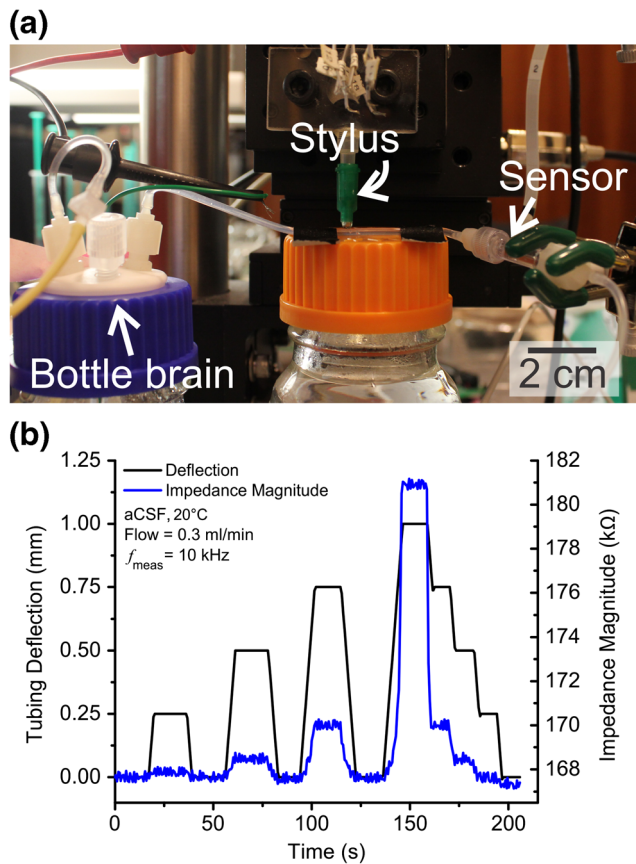
Fig. 14 a Hydrogen peroxide plasma sterilization had no effect on the patency curve of the inline module. **b** Electrochemical impedance spectroscopy and **c** cyclic voltammetry measurements of patency electrode packaged in inline module pre and post H_2O_2 plasma sterilization. Results indicate to changes to the electrode surface properties following sterilization

(a)

(b)

Fig. 15 **a** Image of catheter-occluding experiment to model obstruction of the lumen of the catheter using a stylus. **b** Observed sensor response to catheter deflection using a stylus to close off the lumen. Results indicate that the sensor response varies inversely due to changes in the cross sectional area between the electrodes due to lumen obstruction

electrochemical impedance spectroscopy (EIS; 1× PBS, 1–1,000,000 Hz, Ag/AgCl reference) and cyclic voltammetry (CV; 1×PBS, −0.2 to 1.2 V, scan rate of 250 mV/s for 30 cycles, Ag/AgCl reference) also indicated no changes in electrode surface area or properties following sterilization (Fig. 14b,c), further demonstrating the compatibility of the sterilization process for Parylene-based free film devices. External studies of sterilization efficacy (HIGHPOWER Validation Testing & Lab Services Inc., Rochester, NY) validated the sterilization process of the inline modules using the Sterrad system.

5.8 Dynamic obstruction studies

The ability of the sensor to measure dynamic blockages in the benchtop system was assessed using three different benchtop models of dynamic blockage to mimic expected obstruction phenomena *in vivo*. Initial dynamic blockage experiments were carried out by pinching the catheter line to effectively obstruct the lumen of the catheter using an external stylus probe (Fig. 15a). These experiments not only illustrated the dynamic response of the sensor, but also demonstrated the

sensor response to blockages of the lumen of the catheter, one of the predominant causes for shunt obstructive failure. For this phenomenon, the response of the sensor was found to model the $1/A$ of Eq. 1 (due to changes in the cross sectional area of the ionic conductive path), with the impedance changes increasing as the lumen is obstructed (Fig. 15b).

For a more surface-based obstruction study, a 16-holed catheter was placed within a beaker of aCSF, and transient blockages were simulated by sheathing/unsheathing the drainage ports using larger diameter tubing while patency was continuously monitored. Results indicated that the sensor was capable of repeatedly measuring blockage events over time (Fig. 16). Time constants observed in the settling of the measured impedance is due to the sheathing mechanics of the larger diameter tubing being placed over the 16 holes to impede the conduction paths between the pair of electrodes.

Finally, a "reverse obstruction model" was explored using PEG to obstruct specific holes of a 16-hole mock catheter, then tracking changes in patency during the dissolution of the PEG within aCSF. This technique offered effective control
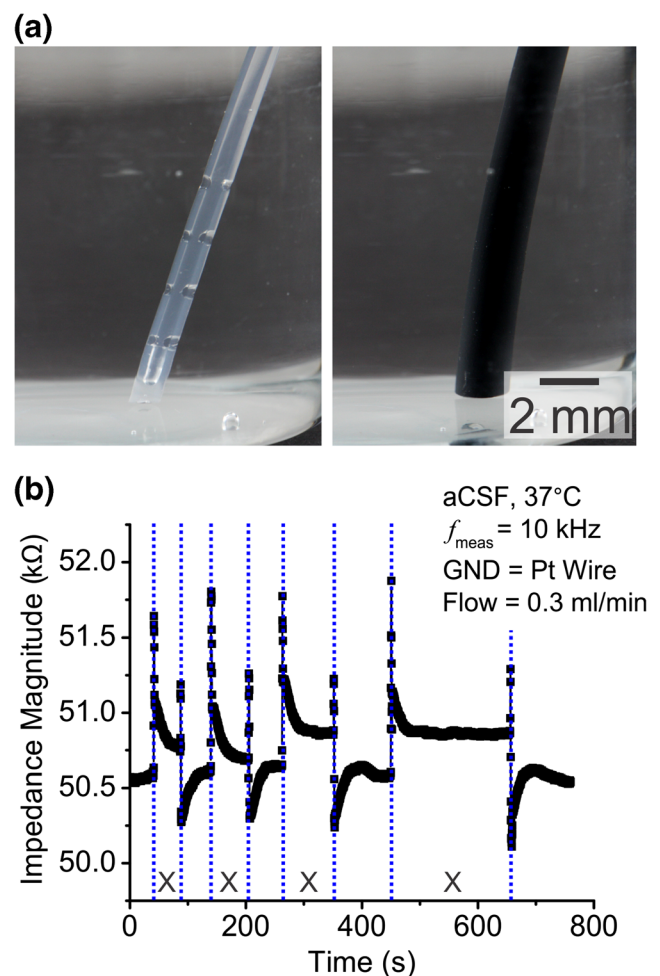
(a)

(b)

Fig. 16 **a** Transient blockage experiments of sheathing/unsheathing a 16-holed catheter illustrated **b** real-time measurement capabilities of the sensors. Obstruction events are labeled with an X
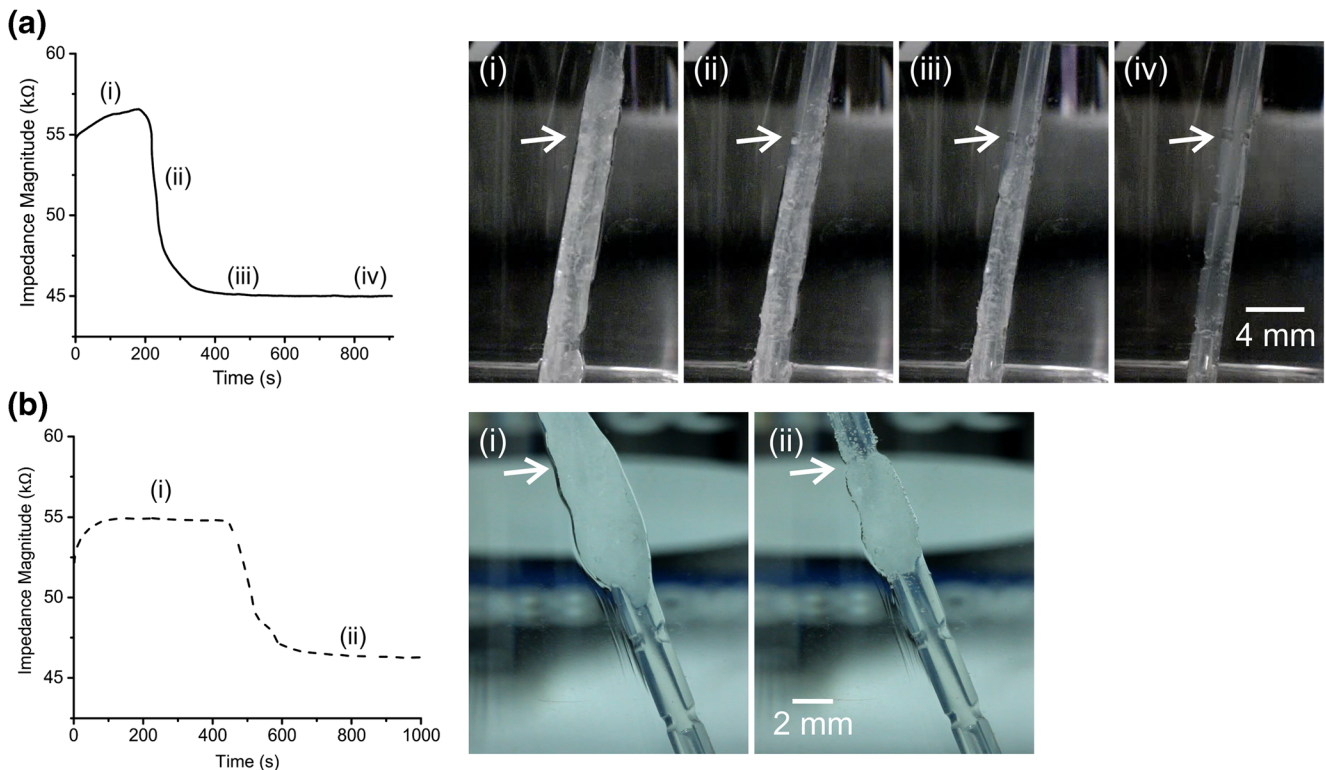
Fig. 17 Dynamic obstruction study using PEG coated mock catheters in aCSF, demonstrating tracking of PEG dissolution ("reverse blockage") using sensor. **a** In the first experiment, all holes of the catheter except for the most distal hole were covered with PEG and sensor response was measured during PEG dissolution. (i) PEG coated catheter is placed in aCSF, (ii) PEG dissolves from the most proximal hole, (iii) only the most proximal hole is open, (iv) all holes are open. [Position of most proximal hole is marked by an arrow.] These results confirm the dependence of the sensor on the position of the most proximal hole. **b** The second experiment revealed a similar response although only the most proximal hole was covered with PEG

over blockage occurrences along the different holes of the catheters. In the first experiment, all holes of the mock catheter except for the most distal hole were covered with a dip-coated layer of PEG and was placed within a beaker of aCSF; a plot of the time varying patency signal as well as corresponding images can be seen in Fig. 17a. For this experiment, impedance maintained a high magnitude (due to the PEG blockage

of catheter holes) until the initial dissolution of the most proximal hole. Dissolution at this hole occurred first due to the dip coating method, which resulted in a thinner coating near the proximal end of the catheter and was confirmed through optical imaging. This dissolution created a sharp decrease in the impedance magnitude (region ii), until the PEG was fully dissolved at the most proximal hole (region iii). Following this, the impedance maintained a constant value even after all the holes were opened (region iv), indicating the dependence of the sensor response on the patency of the most proximal hole as discussed in the previous sections. This result is further evidenced by a second experiment in which only the most proximal hole was covered with PEG and the rest were left open (Fig. 17b). A similar shape in the impedance response to this dissolution study illustrates that the top-most hole is the most critical for the sensor response, and the contribution of the remaining holes is nearly nonexistent.
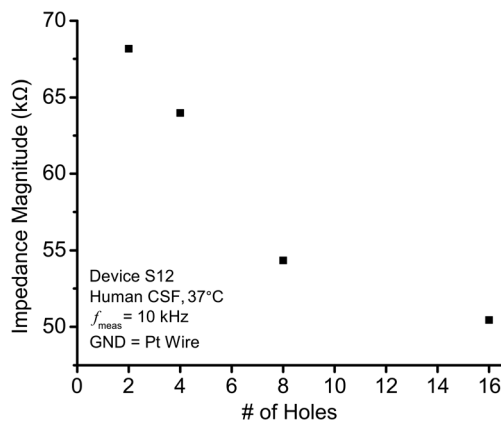
5.9 Human CSF studies

Sensor characterization was also carried out in de-identified, discarded human CSF obtained from patients

Fig. 18 Patency curve for device S12 tested in human CSF solution indicating comparable baseline impedance and sensitivity performance to previous experiments in aCSF

from Los Angeles County and University of Southern California (USC) Hospital. Human CSF was obtained using USC Institutional Review Board (IRB) approved protocols and all experiments were conducted per USC Institutional Biosafety Committee (IBC) approved procedures (IRB# HS-14-00,608, USC IBC# BUA-15-00,026). In these experiments, a patency curve was obtained with the human CSF maintained at 37 °C with continuous mixing to allow for homogeneity of the solution. Qualitatively, the CSF sample was comprised of CSF, blood components (due to subarachnoid hemorrhage), as well as cellular and tissue debris. Baseline impedance measurements for a 16-holed catheter was slightly higher than that observed in aCSF likely due to the increase concentration of blood proteins and tissue, but was still comparable to aCSF baseline values. These results validated the ionic make-up of the aCSF used in previous characterization experiments as an electrochemical model for CSF. Sensor response was identical to characterization of the sensor using aCSF, 35 % impedance increase for 87.5 % blockage (Fig. 18), which is promising moving towards *in vivo* experiments in animals as well as humans with the EVDs.

6 Conclusions

The design, fabrication, packaging, and benchtop characterization of the MEMS electrochemical patency sensor to predict obstruction of ventricular shunts was presented. A cap and inline module for integration of the sensor with current catheter systems was developed for testing, and sensor performance after sterilization and with varying temperature and flow constraints were validated. The preservation of sensor dynamics and response with human CSF further supported benchtop results with aCSF. This patency sensor still needs additional characterization especially given the effect of sensor partiality to the most proximal hole. Despite this, current implantable shunt technologies can benefit greatly through the continuous monitoring of shunt patency. Specifically with the presented sensor, an implantable module is envisioned that houses the inner electrode of the patency sensor within a fluidic channel that is inline between the proximal catheter and valve. The outer electrode may be placed on the external surface of the module or integrated on the external wall of the proximal catheter. The module would also house the corresponding electronics for patency measurement and data capture/transmission. This inline module would then be implanted alongside the catheter/valve system as an extension or fluidic via between the two elements to provide patency data. This integration of patency sensors into shunts will enable quantitative monitoring of shunt performance and more importantly, provide accurate and timely diagnosis of impending failure to improve treatment for hydrocephalus patients.

References

H. E. Ayliffe, R. D. Rabbitt, Measurement Science and Technology **14**(8), 1321 (2003)

J. S. Baru, D. A. Bloom, K. Muraszko, C. E. Koop, J Am Coll Surgeons **192**(1), 79–85 (2001)

S. Basati, K. Tangen, Y. Hsu, H. Lin, D. Frim, A. Linninger. doi: 10.1109/TBME.2014.2335171 (2014)

C. Blegvad, A. Skjolding, H. Broholm, H. Laursen, M. Juhler, Acta Neurochir **155**(9), 1763–1772 (2013)

T. Bork, A. Hogg, M. Lempen, D. Müller, D. Joss, T. Bardyn, P. Büchler, H. Keppner, S. Braun, Y. Tardy, Biomed Microdevices **12**(4), 607–618 (2010)

S. R. Browd, B. T. Ragel, O. N. Gottfried, J. R. W. Kestle, Pediatric Neurology **34**(2), 83–92 (2006)

H. L. Brydon, G. Keir, E. J. Thompson, R. Bayston, R. Hayward, W. Harkness, Journal of Neurology, Neurosurgery & Psychiatry **64**(5), 643–647 (1998)

W. H. Coulter, In: Proc Natl Electron Conf, 1034–1040 (1956)

R. D. Dickerman, W. J. McConathy, J. Morgan, Q. E. Stevens, J. T. Jolley, S. Schneider, M. A. Mittler, J Clin Neurosci **12**(7), 781–783 (2005)

J. M. Drake, J. R. Kestle, R. Milner, G. Cinalli, F. Boop, J. Piatt Jr., S. Haines, S. J. Schiff, D. D. Cochrane, P. Steinbok, Neurosurgery **43**(2), 294–303 (1998)

J. Drake, J. Kestle, S. Tuli, Child's Nervous System **16**(10–11), 800–804 (2000)

C.A. Gutierrez, E. Meng. J Microelectromech S 20 5, 1098–1108 (2011)

C.A. Gutierrez, C. Lee, B. Kim, E. Meng. In: Solid-State Sensors, Actuators and Microsystems Conference (TRANSDUCERS), 16th International, 5–9 June 2011 2011. pp 2299–2302 (2011)

E. J. Haberl, M. Messing-Juenger, M. Schuhmann, R. Eymann, C. Cedzich, M. J. Fritsch, M. Kiefer, E. J. Van Lindert, C. Geyer, M. Lehner, Journal of Neurosurgery: Pediatrics **4**(3), 288–293 (2009)

C. A. Harris, J. P. McAllister II, Child's Nervous System **27**(8), 1221–1232 (2011)

C. A. Harris, J. P. McAllister, Neurosurgery **70**(6), 1589–1602 (2012)

C. A. Harris, J. H. Resau, E. A. Hudson, R. A. West, C. Moon, J. P. McAllister, Exp Neurol **222**(6), 204–210 (2010)

C. A. Harris, J. H. Resau, E. A. Hudson, R. A. West, C. Moon, A. D. Black, J. P. McAllister, J Biomed Mater Res Part A **97**(4), 433–440 (2011)

B. A. Kaufman, T. Park, Pediatric Neurosurgery **31**(1), 1–6 (1999)

J. Kestle, J. Drake, R. Milner, C. Sainte-Rose, G. Cinalli, F. Boop, J. Piatt, S. Haines, S. Schiff, D. Cochrane, P. Steinbok, N. MacNeil, Pediatric Neurosurgery **33**(5), 230–236 (2000)

B.J. Kim, C.A. Gutierrez, G.A. Gerhardt, E. Meng. In: Micro Electro Mechanical Systems (MEMS), 2012 I.E. 25th International Conference on, Jan. 29 2012-Feb. 2 2012 pp 124–127 (2012)

A. V. Kulkarni, J. M. Drake, M. Lamberti-Pasculli, J Neurosurg **94**(2), 195–201 (2001)

J. Lin, M. Morris, W. Olivero, F. Boop, R. A. Sanford, J Neurosurg **99**(2), 426–431 (2003)

F. Lundberg, D.-Q. Li, D. Falkenback, T. Lea, P. Siesjö, S. Söderström, B. J. Kudryk, J. O. Tegenfeldt, S. Nomura, Å. Ljungh, J Neurosurg **90**(1), 101–108 (1999)

B. R. Lutz, P. Venkataraman, S. R. Browd, Surgical Neurology International **4**(Suppl 1), S38 (2013)

E. Meng, P. Y. Li, Y. C. Tai, J. Micromech. Microeng. **18**, 4 (2008)

E. Meng, X. Zhang, W. Benard, in *R Ghodssi*, ed by P. Li. Additive processes for polymeric materials (Springer, Mems Materials and Processes Handbook, 2011), pp. 193–271

Y. Nam, MRS bulletin **37**(06), 566–572 (2012)

I. K. Pople, Journal of neurology. Neurosurgery & Psychiatry **73**(suppl 1), i17–i22 (2002)

R. Sheybani, N.E. Cabrera-Munoz, T. Sanchez, E. Meng. In: Engineering in Medicine and Biology Society (EMBC), Annual International Conference of the IEEE, Aug. 28 2012-Sept. 1 2012 2012. pp 519–522 (2012)

U. W. Thomale, H. Hosch, A. Koch, M. Schulz, G. Stoltenburg, E.-J. Haberl, C. Sprung, Child's Nervous System **26**(6), 781–789 (2010)

S. Tuli, B. O'Hayon, J. Drake, M. Clarke, J. Kestle, Neurosurgery **45**(6), 1329 (1999)

J. M. Wong, J. E. Ziewacz, A. L. Ho, J. R. Panchmatia, A. M. Bader, H. J. Garton, E. R. Laws, A. A. Gawande, Neurosurgical Focus **33**(5), E13 (2012)